

powder size (see Supplementary Information for details). This increase is entirely due to coarsening in the first-step sintering. As nanocrystalline powders in the size range 5–10 nm are becoming increasingly available^{24,25}, we believe that it should be possible to achieve dense, nanostructured materials of grain size 25–50 nm by exploiting the kinetic ‘window’ that separates grain-boundary diffusion from grain growth. We consider that the simplicity of this approach should also make it useful for detailed explorations of dense nanostructured materials, in order to take advantage of their grain-size-dependent physical properties. □

Methods

We used a precipitation technique to first obtain Y(OH)₃, which was then calcined at various temperatures from 600 to 800 °C to obtain final Y₂O₃ powders with a size from 10 to 100 nm. These powders were sifted and pressed into pellets. When doping was desired, Mg and Nb salts were introduced to aqueous slurries of Y₂O₃ powders; the slurries were gelled by adjusting their pH, then dried and recalcined. The pellets were sintered in a dilatometer or in a box furnace in air. The final density was determined using Archimedes’ method and quantitative microscopy.

Received 31 August 1999; accepted 17 January 2000.

1. Coble, R. L. Sintering crystalline solids. *J. Appl. Phys.* **32**, 787–799 (1961).
2. Coble, R. L. & Burke, J. E. in *Progress in Ceramic Science* Vol. 3 (ed. Burke, J. E.) 197–251 (New York, 1963).
3. Brook, R. J. in *Treatise on Materials Science and Technology* Vol. 9 (ed. Wang, F. F. Y.) 331–363 (Academic, New York, 1976).
4. Coble, R. L. & Cannon, R. M. in *Processing of Crystalline Ceramics* (ed. Palmour, H. III) 151–168 (Materials Science Research Vol. 11, Plenum, New York, 1978).
5. Coble, R. L., Song, H., Brook, R. J., Handwerker, C. A. & Dynys, J. M. in *Structure and Properties of MgO and Al₂O₃ Ceramics* (ed. Kingery, W. D.) 839–852 (Vol. 10, Advances in Ceramics, American Ceramic Society, Westerville, OH, 1984).
6. Cameron, C. P. & Raj, R. Grain growth transition during sintering of colloiddally prepared alumina powder compacts. *J. Am. Ceram. Soc.* **71**, 1031–1035 (1988).
7. Gleiter, H. Nanocrystalline materials. *Prog. Mater. Sci.* **33**, 223–315 (1989).
8. Mayo, M. J. Processing of nanocrystalline ceramics from ultrafine particles. *Int. Mater. Rev.* **41**, 85–115 (1996).
9. Liao, S.-C., Chen, Y.-J., Kear, B. H. & Mayo, W. E. High pressure/low temperature sintering of nanocrystalline alumina. *Nanostruct. Mater.* **10**, 1063–1079 (1998).
10. Chen, P.-L. & Chen, I.-W. Grain boundary mobility in Y₂O₃: defect mechanism and dopant effects. *J. Am. Ceram. Soc.* **79**, 1801–1809 (1996).
11. Chen, P.-L. & Chen, I.-W. Sintering of fine oxide powder: I, microstructural evolution. *J. Am. Ceram. Soc.* **79**, 3129–3141 (1996).
12. Chen, P.-L. & Chen, I.-W. Sintering of fine oxide powders: II, sintering mechanisms. *J. Am. Ceram. Soc.* **80**, 637–645 (1997).
13. Kingery, W. D. & Francois, B. in *Sintering and Related Phenomena* (eds Kuczynski, G. C., Hooton, N. S. & Gibbon, C. F.) 471–496 (Gordon & Breach, New York, 1967).
14. McFadden, S. X., Mishra, R. S., Valiev, R. Z., Zhilyaev, A. P. & Mukherjee, A. K. Low-temperature superplasticity in nanostructured nickel and metal alloys. *Nature* **396**, 684–686 (1999).
15. Wakai, F. et al. A superplastic covalent crystal composite. *Nature* **344**, 421–423 (1990).
16. Chen, I.-W. & Xue, L.-A. Development of superplastic structure ceramics. *J. Am. Ceram. Soc.* **73**, 2585–2609 (1990).
17. Herring, C. Effect of change of scale on sintering phenomena. *J. Appl. Phys.* **21**, 301–303 (1950).
18. Zhao, J. & Harmer, M. P. Sintering of ultra-high purity alumina doped simultaneously with MgO and FeO. *J. Am. Ceram. Soc.* **70**, 860–866 (1987).
19. Hansen, J. D., Rusin, R. P., Teng, M.-H. & Johnson, D.-L. Combined stage sintering model. *J. Am. Ceram. Soc.* **75**, 1129–1135 (1992).
20. Czubyko, L., Sursavaeva, V. G., Gottstein, G. & Shvindlerman, L. S. Influence of triple junctions on grain boundary motion. *Acta Mater.* **46**, 5863–5871 (1998).
21. Land, T. A., Martin, T. L., Potapenko, S., Palmore, G. T. & De Yoreo, J. J. Recovery of surfaces from impurity poisoning during crystal growth. *Nature* **399**, 442–445 (1999).
22. Cannon, R. M., Rhodes, W. H. & Heuer, A. H. Plastic deformation of fine-grained alumina: I. interface-controlled diffusional creep. *J. Am. Ceram. Soc.* **63**, 48–53 (1980).
23. Arzt, E., Ashby, M. F. & Verrall, R. A. Interface-controlled diffusional creep. *Acta Metall.* **31**, 1977–1989 (1983).
24. Kumar, K. P. et al. Densification of nanostructured titania assisted by a phase transformation. *Nature* **358**, 48–51 (1992).
25. Klein, S., Winterer, M. & Hahn, H. Reduced pressure chemical vapor synthesis of nano-crystalline silicon carbide powders. *Adv. Mater.* **4**, 143–149 (1998).

Supplementary information is available on Nature’s World-Wide Web site or as paper copy from the London editorial office of Nature.

Acknowledgements

This work was supported by the US Department of Energy, Office of Basic Energy Sciences, using facilities supported by the NSF MRSEC at the University of Pennsylvania.

Correspondence and requests for materials should be addressed to I.-W.C. (e-mail: iweichen@seas.upenn.edu).

The influence of Antarctic sea ice on glacial–interglacial CO₂ variations

Britton B. Stephens*† & Ralph F. Keeling*

* Scripps Institution of Oceanography, University of California, San Diego, La Jolla, California 92093–0244, USA

Ice-core measurements indicate that atmospheric CO₂ concentrations during glacial periods were consistently about 80 parts per million lower than during interglacial periods¹. Previous explanations for this observation^{2–9} have typically had difficulty accounting for either the estimated glacial O₂ concentrations in the deep sea, ¹³C/¹²C ratios in Antarctic surface waters, or the depth of calcite saturation; also lacking is an explanation for the strong link between atmospheric CO₂ and Antarctic air temperature¹. There is growing evidence that the amount of deep water upwelling at low latitudes is significantly overestimated in most ocean general circulation models^{10,11} and simpler box models previously used to investigate this problem. Here we use a box model with deep-water upwelling confined to south of 55 °S to investigate the glacial–interglacial linkages between Antarctic air temperature and atmospheric CO₂ variations. We suggest that low glacial atmospheric CO₂ levels might result from reduced deep-water ventilation associated with either year-round Antarctic sea-ice coverage, or wintertime coverage combined with ice-induced stratification during the summer. The model presented here reproduces 67 parts per million of the observed glacial–interglacial CO₂ difference, as a result of reduced air–sea gas exchange in the Antarctic region, and is generally consistent with the additional observational constraints.

Most theories for low glacial atmospheric CO₂ concentrations rely on one of two mechanisms: an increase in the strength of the biological pump as a result of changes in the supply or utilization of nutrients or light^{2–6}, or an increase in the ocean’s alkalinity via coral reef dissolution⁷ or carbonate sediment interactions^{8,9}. Models that invoke biological pump changes are generally inconsistent with the magnitude and/or direction of glacial–interglacial changes in ¹³C/¹²C ratios and nutrients^{12,13}, and with the lack of widespread glacial deep-water anoxia. On the other hand, models invoking alkalinity changes predict large increases in the depth of the glacial lysocline which are not observed.

Our model is not based on productivity or alkalinity increases, but rather on changes in the rate of air–sea gas exchange as a result of increased sea-ice cover at high southern latitudes. By significantly limiting the sea-to-air CO₂ flux in the primary region for deep-water ventilation, expanded Antarctic sea ice during glacial times may trap relatively more carbon in the deep ocean, thereby reducing atmospheric CO₂ concentrations. This mechanism would increase the effectiveness of the biological pump at storing CO₂ in the deep ocean without actually increasing productivity, and thus would not necessarily require changes in nutrient concentrations or utilization efficiencies. Because dissolved O₂ equilibrates with the atmosphere more rapidly than CO₂, as a result of its lack of buffering chemistry, the limitation imposed by glacial sea ice would have a lesser effect on O₂ entering the deep ocean than on CO₂ leaving, and thus would not produce deep anoxia. Furthermore, increased Antarctic sea ice would not produce a large lysocline shift. Finally, the direct connections between Antarctic temperature and sea-ice cover provide a possible explanation for the observed synchrony between Antarctic temperature and atmospheric CO₂ concentrations during deglaciation⁶.

† Present address: Cooperative Institute for Research in Environmental Sciences, University of Colorado at Boulder, Boulder, Colorado 80309–0216, USA.

Increases in Antarctic sea ice have been included in three-dimensional ocean model simulations, but their potential to significantly affect atmospheric CO₂ in these models may be limited by defects involving excessive low-latitude upwelling of deep water. Toggweiler and Samuels¹⁰ have shown from ¹⁴C comparisons, and Gnanadesikan and Toggweiler¹¹ from silica flux comparisons, that coarse-resolution ocean models all overestimate the amount of deep water upwelling across the main thermocline at low latitudes in the Indian and Pacific oceans. Previous box models used to explore palaeo-CO₂ controls^{2–4,14,15} also overestimate deep-water upwelling at low latitudes. These models have from 15 to 40 Sv (1 Sv = 10⁶ m³ s⁻¹) of upwelling directly from the deep to the warm surface box, which is much greater than the combined upper limit of ~7 Sv indicated by tracer and transect studies in the Pacific¹⁰ and Indian¹⁶ oceans.

To investigate the influence of Antarctic sea ice in the absence of low-latitude deep-water upwelling, we employ the biogeochemical ocean model shown in Fig. 1. The fundamental difference between this and other box models of the ocean carbon cycle is that deep waters only return to the surface south of the Antarctic Polar Front (APF), consistent with the “reconfigured conveyor” of Toggweiler and Samuels¹⁰. We divide the upper ocean into a warm, low-nutrient surface (S) box and a cooler, higher-nutrient thermocline (T) box. We also separate the upwelling that feeds the Antarctic Bottom Water (AABW) formation (B) box from that which flows north in

the Antarctic surface (A) box to allow for higher nutrient concentrations in AABW¹⁷. We selected these divisions to optimize the model’s representation of the modern distribution of preformed nutrients and export production. However, combining either the B and A boxes or the S and T boxes does not change our results significantly.

Deep waters that upwell along the Antarctic Divergence, mix with surface waters, and then flow north are generally thought to sink again at the APF as part of the low-salinity Antarctic Intermediate Water (AAIW)¹⁸. Although there is considerable uncertainty^{19,20}, it appears that some of this recent deep water remains near the surface north of the APF where it convectively mixes with surface waters of low-latitude origin before sinking. To investigate model sensitivities to uncertainties in the fate of northward-flowing Antarctic surface waters, we allow for surface exposure of an adjustable fraction (F_a) of these waters in the subantarctic (SA) box.

After prescribing temperatures, salinities, water transports, and surface nutrients, and parametrizing the effects of biological production, air–sea gas exchange, and carbonate sediment interaction, we integrate the model to calculate the steady-state distribution of total CO₂ (Σ CO₂), the ¹³C/¹²C ratio (δ^{13} C), total alkalinity (TA), dissolved O₂, and the atmospheric CO₂ concentration. Figure 1 depicts a solution to this model using input parameters representing the modern pre-industrial state. To assess the sensitivity of our model to variations in Antarctic ice cover, we have calculated

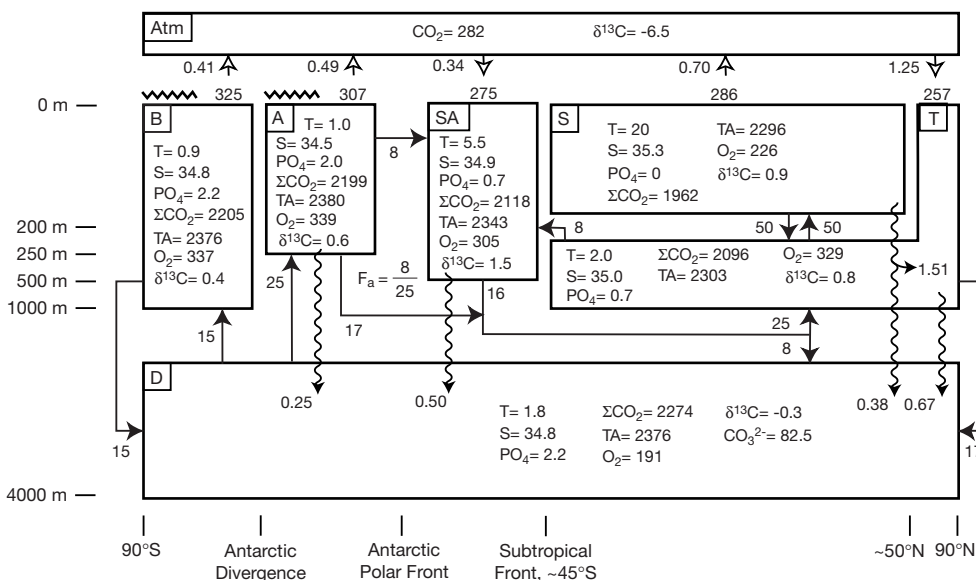


Figure 1 Solution from our atmosphere–ocean model for a best-guess modern-preindustrial state. In this state, $F_a = 0.3$, where F_a is the fraction of northward-flowing Antarctic surface waters exposed to the surface in the subantarctic (SA) box. This model consists of an atmosphere and six ocean boxes: a main surface box (S) representing the upper 200 m of water between approximately 50°N and the Southern Subtropical Front (STF), a main thermocline box (T) representing waters between 200 and 1,000 m depth with a surface outcrop north of the main surface box, an Antarctic Bottom Water formation box (B) representing the upper 1,000 m of water south of the Antarctic Divergence (AD) (~65°S today), an Antarctic surface box (A) representing the upper 250 m of the Southern Ocean south of the APF (~55°S today) and north of the AD, a subantarctic box (SA) representing the upper 500 m of water north of the APF and south of the STF, and a deep box (D) representing the remainder of the world’s oceans. Solid straight arrows denote water fluxes and are labelled in Sv. Solid wavy arrows indicate sinking fluxes of organic material and hollow arrows indicate air–sea CO₂ fluxes, and both are labelled in Gt C yr⁻¹. Numbers above the surface boxes denote CO₂ partial pressures in μ atm. Values for PO₄, Σ CO₂, TA, dissolved O₂, and CO₃²⁻ are indicated in μ mol kg⁻¹, δ^{13} C in per mil, temperature T in °C, salinity S in p.s.u., and atmospheric CO₂ in p.p.m. We assume that 50% of the modern-preindustrial ocean in boxes B and A is covered by sea-ice

(represented by jagged lines), leaving a combined area of 1.6×10^{13} m² open for the ventilation of upwelled deep waters. We prescribe surface phosphate concentrations in the A, SA, S and T boxes, and the total ocean phosphate concentration, such that the model reproduces the observed deep preformed phosphate (PO₄³⁻) concentration of 1.4 μ mol kg⁻¹ and the PO₄⁰ concentration of intermediate waters penetrating the deep ocean, also equal to 1.4 μ mol kg⁻¹ (ref. 30). The model consumes excess phosphate in these four surface boxes at revised Redfield proportions of -175 O₂:127 C:16 N:1 P. As the resulting organic matter sinks, 80% of the main surface flux is oxidized in the thermocline box and the remainder of all three fluxes in the deep box. We assume inorganic to organic carbon production ratios of 0, 1:20, 1:10 and 1:3 in the A, SA, S and T boxes respectively. The model remineralizes all sinking calcium carbonate in the deep box. We calculate fluxes across the air–sea interface assuming a perfectly mixed atmosphere and using CO₂ invasion rates of 0.15 (B, A, SA, T) and 0.05 (S) mol m⁻² yr⁻¹ μ atm⁻¹, and O₂ gas transfer velocities of 45 (B, A, SA, T) and 15 (S) cm h⁻¹. We maintain a constant CO₃²⁻ concentration in the deep box by dissolving or precipitating an appropriate amount of CaCO₃ (ref. 8). We have adjusted the mixing between the thermocline and surface boxes to produce a reasonable partitioning of biological productivity between these boxes.

steady-state solutions using these parameters and varying the ice-free surface area south of the APF from $1.6 \times 10^{13} \text{ m}^2$ down to zero. Figure 2a shows the atmospheric CO_2 concentration for these solutions for four cases with different values of F_a .

The decrease in atmospheric CO_2 of 67 parts per million (p.p.m.) for the best-guess conditions shown in Fig. 2 is associated with a 92% decrease in the sea-to-air CO_2 flux south of the APF, and a 1.8% increase in the deep ΣCO_2 concentration, with no change in the nutrient distribution. The deep ΣCO_2 increase contributes to the dissolution of $2.5 \times 10^{16} \text{ mol}$ of CaCO_3 , which produces a 1.6% increase in whole ocean alkalinity and contributes 13 p.p.m. of the total atmospheric CO_2 effect. Although not enough to produce large changes in glacial lysocline depths, this alkalinity-ice relationship is consistent with observations of a global carbonate-sediment preservation spike during deglaciation²¹.

In contrast to atmospheric CO_2 , the modelled deep O_2 concentration is not sensitive to ice coverage except when the outcrop area becomes very small (Fig. 2b). The change in deep O_2 from a modern-preindustrial estimate of $191 \mu\text{mol kg}^{-1}$ to a possible glacial value of $123 \mu\text{mol kg}^{-1}$ (Fig. 2b) would not produce deep anoxia. Our model also supports earlier suggestions^{12,22} that sea ice is an important influence on glacial Antarctic surface $\delta^{13}\text{C}$ values. Fractionation effects associated with both net and gross air-sea CO_2 fluxes work to make the Antarctic surface box richer in ^{13}C . As these fluxes decrease with increasing ice cover, the Antarctic surface $\delta^{13}\text{C}$ value decreases by 0.7‰ (Fig. 2b). This decrease is similar to that inferred from measurements on planktonic foraminifera¹², and is in contrast to the increases in Antarctic surface $\delta^{13}\text{C}$ implied by models that invoke increases in high-latitude nutrient utilization or decreases in high-latitude vertical mixing.

Atmospheric $\delta^{13}\text{C}$ increases with increasing sea ice by 0.9‰ in the best-case model scenario. If we include an input of 500 gigatons of terrestrial carbon²³, and reduce surface temperatures by a maximum of 5°C (ref. 24) and less in boxes that are already near the freezing point—the atmospheric $\delta^{13}\text{C}$ value returns to within 0.1‰ of the modern-preindustrial value. Measurements^{15,25} indicate a sharp dip in atmospheric $\delta^{13}\text{C}$ of ~ 0.5 ‰ at the start of termination I, followed by a more gradual increase to a pre-industrial value several tenths of a per mil above that at the Last Glacial Maximum (LGM). Although our model does not reproduce this overall shift, it does suggest that the temporal behaviour of atmospheric $\delta^{13}\text{C}$ during deglaciation could be explained by an initial meltback of Antarctic sea ice followed by a more gradual growth in terrestrial biomass and increase in surface temperatures.

Although it is difficult to estimate the extent of glacial Antarctic sea ice, suggestions from sediment proxies of significantly increased coverage justify the investigation of its potential implications for atmospheric CO_2 . There is solid evidence from ice-rafted volcanic detritus²⁶, and support from fossil plankton assemblages²⁷, that wintertime Antarctic sea ice extended to or beyond the modern APF during the LGM. However, summertime LGM ice limits are not as well constrained. Early estimates of significantly increased coverage based on sediment types²⁶ have been countered by recent planktonic analyses that suggest summertime Antarctic sea ice at the LGM may not have been much more extensive than today²⁷. For our purposes, we expect the winter ice extent to have the main effect on deep-water ventilation, as stratification and biological productivity during summer independently limit the outgassing of CO_2 and uptake of O_2 . François *et al.*²⁸ used sediment $\delta^{15}\text{N}$ and opal data to estimate that increased stratification south of the APF during glacial times led to a 70% utilization of nutrients. This would be sufficient to remove $196 \mu\text{mol C kg}^{-1}$ ($0.7 \times 127 \times 2.2 \mu\text{mol}$ phosphate per kg) from the Antarctic surface waters, and thus prevent summertime CO_2 outgassing in our model. Furthermore, the extreme reduction in vertical mixing implied by the tenfold decrease in nutrient inputs estimated by François *et al.*²⁸ suggests that a large amount of ice remained in this region throughout the summer.

The results shown in Fig. 2 should be viewed as an indication of a potentially important mechanism in the ocean-atmosphere carbon system, rather than as an absolute prediction of the magnitude of the Antarctic sea-ice effect. However, we note that its magnitude is fairly robust with respect to variations in the assumed parameters. In addition to the sensitivities to ice-free area and F_a shown in Fig. 2a, the best-guess CO_2 difference changes by only -9 p.p.m. or $+10$ p.p.m. if the entrainment of low-latitude waters in AAIW is respectively doubled or reduced to zero. Although our model illustrates the behaviour of the ocean in the limit of no low-latitude deep-water upwelling, it is likely that there is some finite amount of diapycnal flow through the main thermocline in the real ocean. However, if we include a high-latitude sinking, low-latitude upwelling term of 10 Sv in our model, the total atmospheric CO_2 difference decreases by only 8 p.p.m. to a total of 59 p.p.m.

In addition, we have not tried to simulate increases in nutrient utilization in the subantarctic, yet in our model such changes could significantly affect the amount of CO_2 entering the deep ocean. If we reduce subantarctic surface nutrients after increasing Antarctic sea ice to generate an increase from 1.5 to $2.8 \text{ mol C m}^{-2} \text{ yr}^{-1}$ in subantarctic export production (slightly less than that proposed by François *et al.*²⁸), the CO_2 drawdown increases by 15 p.p.m. to a total of 82 p.p.m. A final perturbation to consider is that of temperature-driven solubility changes. After reducing surface temperatures as described above, our model predicts an additional CO_2 drawdown of 27 p.p.m., corresponding to a Harvardton Bear Index²³ of 0.2. The combined effects of ice cover, subantarctic productivity, and temperature simulated by our model are

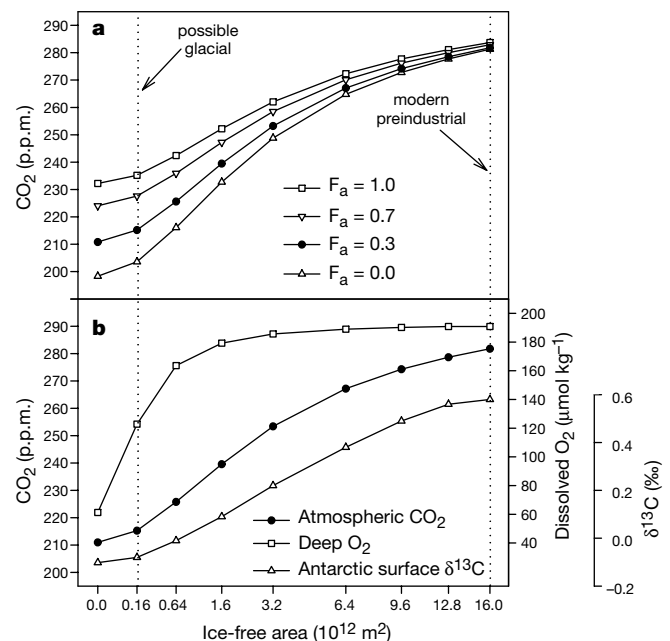


Figure 2 Steady-state model solutions for different ice coverages south of the Antarctic Polar Front (APF). We vary the exposed sea surface in the B and A boxes such that the same fraction of total surface is ice-free in each. The x-axis values represent the sum of exposed area in these two boxes, and are scaled by their square root to expand the left side of the plot. We use $1.6 \times 10^{13} \text{ m}^2$ as a modern estimate of the ice-free area south of the APF, and $1.6 \times 10^{11} \text{ m}^2$ to illustrate a possible glacial value. **a**, Atmospheric CO_2 using modern-preindustrial parameters and different fractions (F_a) of Antarctic surface waters entering the subantarctic box. Based on the evidence of Molinelli¹⁹ showing the importance of subsurface transport of Antarctic waters relative to vertical mixing as the subantarctic source of AAIW, we have chosen a relatively low F_a value of 0.3 to use as a best-guess case. **b**, Atmospheric CO_2 , deep O_2 , and Antarctic surface $\delta^{13}\text{C}$ using $F_a = 0.3$.

sufficiently large to ensure that an 80 p.p.m. decrease in glacial atmospheric CO₂ can still be attained even after including the counteracting effects of terrestrial biomass changes and salinity-driven solubility effects²³. Toggweiler²⁹ recently developed a model that similarly invokes a reduction in deep-water ventilation to explain the low glacial CO₂ levels. Whereas he generates reduced ventilation by decreasing the vertical exchange between deep and Antarctic surface waters, we suggest that reduced ventilation was driven by limitations to air–sea gas exchange imposed by increased sea ice in this region. □

Received 13 May 1999; accepted 18 January 2000.

- Petit, J. R. *et al.* Climate and atmospheric history of the past 420,000 years from the Vostok ice core, Antarctica. *Nature* **399**, 429–436 (1999).
- Sarmiento, J. L. & Toggweiler, J. R. A new model for the role of the oceans in determining atmospheric pCO₂. *Nature* **308**, 621–624 (1984).
- Siegenthaler, U. & Wenk, T. Rapid atmospheric CO₂ variations and ocean circulation. *Nature* **308**, 624–626 (1984).
- Knox, F. & McElroy, M. B. Changes in atmospheric CO₂: Influence of the marine biota at high latitude. *J. Geophys. Res.* **89**, 4629–4637 (1984).
- Martin, J. H. Glacial–interglacial CO₂ change: The iron hypothesis. *Paleoceanography* **5**, 1–13 (1990).
- Broecker, W. S. & Henderson, G. M. The sequence of events surrounding Termination II and their implications for the cause of glacial–interglacial CO₂ changes. *Paleoceanography* **13**, 352–364 (1998).
- Opydyke, B. N. & Walker, J. C. G. Return of the coral reef hypothesis: Basin to shelf partitioning of CaCO₃ and its effect on atmospheric CO₂. *Geology* **20**, 733–736 (1982).
- Boyle, E. A. The role of vertical chemical fractionation in controlling Late Quaternary atmospheric carbon dioxide. *J. Geophys. Res.* **93**, 15701–15714 (1988).
- Archer, D. & Maier–Reimer, E. Effect of deep-sea sedimentary calcite preservation on atmospheric CO₂ concentration. *Nature* **367**, 260–263 (1994).
- Toggweiler, J. R. & Samuels, B. in *The Global Carbon Cycle* (ed. Heimann, M.) 333–366 (Springer, Berlin, 1993).
- Gnanadesikan, A. & Toggweiler, J. R. Constraints placed by silicon cycling on vertical exchange in general circulation models. *Geophys. Res. Lett.* **26**, 1865–1868 (1999).
- Charles, C. D. & Fairbanks, R. G. in *Geological History of the Polar Oceans: Arctic Versus Antarctic* (eds Bleil, U. & Thiede, J.) 519–538 (Kluwer Academic, Dordrecht, 1990).
- Boyle, E. A. Cadmium and δ¹³C paleochemical ocean distributions during the Stage 2 glacial maximum. *Annu. Rev. Earth Planet. Sci.* **20**, 245–287 (1992).
- Toggweiler, J. R. & Sarmiento, J. L. in *The Carbon Cycle and Atmospheric CO₂: Natural Variations Archean to Present* (eds Sundquist, E. T. & Broecker, W. S.) 163–184 (American Geophysical Union, Washington DC, 1985).
- Marino, B. M., McElroy, M. B., Salawitch, R. J. & Spaulding, W. G. Glacial-to-interglacial variations in the carbon isotopic composition of atmospheric CO₂. *Nature* **357**, 461–466 (1992).
- Robbins, P. E. & Toole, J. M. The dissolved silica budget as a constraint on the meridional overturning circulation of the Indian Ocean. *Deep-Sea Res.* **44**, 879–906 (1997).
- Broecker, W. S. *et al.* How much deep water is formed in the Southern Ocean? *J. Geophys. Res.* **103**, 15833–15843 (1998).
- Tomczak, M. & Godfrey, J. S. *Regional Oceanography: An Introduction* 67–87 (Pergamon, Oxford, 1994).
- Molinelli, E. J. The Antarctic influence on Antarctic Intermediate Water. *J. Mar. Res.* **39**, 267–293 (1981).
- McCartney, M. S. in *A Voyage of Discovery* (ed. Angel, M.) 103–119 (Pergamon, Oxford, 1977).
- Berger, W. H. Deep-sea carbonate and the deglaciation preservation spike in pteropods and foraminifera. *Nature* **269**, 301–304 (1977).
- Broecker, W. S. An oceanographic explanation for the apparent carbon isotope–cadmium discordancy in the glacial Antarctic? *Paleoceanography* **8**, 137–139 (1993).
- Broecker, W. S. & Peng, T.-H. *Greenhouse Puzzles* 2nd edn (Eldigio, Palisades, New York, 1998).
- Guilderson, T. P., Fairbanks, R. G. & Rubinstone, J. L. Tropical temperature variations since 20,000 years ago: Modulating interhemispheric climate change. *Science* **263**, 663–665 (1994).
- Smith, H. J., Fischer, H., Wahlen, M., Mastroianni, D. & Deck, B. Dual modes of the carbon cycle since the Last Glacial Maximum. *Nature* **400**, 248–250 (1999).
- Cooke, D. W. & Hays, J. D. in *Antarctic Geoscience: Symposium on Antarctic Geology and Geophysics* (ed. Craddock, C.) 1017–1025 (University of Wisconsin Press, Madison, Wisconsin, 1982).
- Crosta, X., Pichon, J.-J. & Burckle, L. H. Reappraisal of Antarctic seasonal sea-ice at the Last Glacial Maximum. *Geophys. Res. Lett.* **26**, 1865–1868 (1999).
- François, R. *et al.* Contribution of Southern Ocean surface-water stratification to low atmospheric CO₂ concentrations during the last glacial period. *Nature* **389**, 929–935 (1997).
- Toggweiler, J. R. Variation of atmospheric CO₂ by ventilation of the ocean's deepest water. *Paleoceanography* **14**, 571–588 (1999).
- Broecker, W. S., Takahashi, T. & Takahashi, T. Sources and flow patterns of deep-ocean waters as deduced from potential temperature, salinity, and initial phosphate concentration. *J. Geophys. Res.* **90**, 6925–6939 (1985).

Acknowledgements

We thank R. Toggweiler, J. Sarmiento, C. Charles and J. Severinghaus for helpful discussions. This work was supported by the National Science Foundation and the Achievement Rewards for College Scientists Foundation.

Correspondence and requests for materials should be addressed to B.B.S. at the University of Colorado at Boulder (e-mail: britt@cmdl.noaa.gov).

Interferometric radar measurements of water level changes on the Amazon flood plain

Douglas E. Alsdorf*, John M. Melack*†, Thomas Dunne†, Leal A. K. Mertes*‡, Laura L. Hess* & Laurence C. Smith§

* Institute for Computational Earth System Science, University of California, Santa Barbara, California 93106, USA

† Donald Bren School of Environmental Science and Management, University of California, Santa Barbara, California 93106, USA

‡ Department of Geography, University of California, Santa Barbara, California 93106, USA

§ Department of Geography, University of California, Los Angeles, California 90095, USA

Measurements of water levels in the main channels of rivers, upland tributaries and floodplain lakes are necessary for understanding flooding hazards, methane production, sediment transport and nutrient exchange. But most remote river basins have only a few gauging stations and these tend to be restricted to large river channels. Although radar remote sensing techniques using interferometric phase measurements have the potential to greatly improve spatial sampling, the phase is temporally incoherent over open water and has therefore not been used to determine water levels. Here we use interferometric synthetic aperture radar (SAR) data^{1–3}, acquired over the central Amazon by the Space Shuttle imaging radar mission⁴, to measure subtle water level changes in an area of flooded vegetation on the Amazon flood plain. The technique makes use of the fact that flooded forests and floodplain lakes with emergent shrubs permit radar double-bounce returns from water and vegetation surfaces^{5,6}, thus allowing coherence to be maintained. Our interferometric phase observations show decreases in water levels of 7–11 cm per day for tributaries and lakes within ~20 km of a main channel and 2–5 cm per day at distances of ~80 km. Proximal floodplain observations are in close agreement with main-channel gauge records, indicating a rapid response of the flood plain to decreases in river stage. With additional data from future satellite missions, the technique described here should provide direct observations important for understanding flood dynamics and hydrologic exchange between rivers and flood plains.

Climatically driven, seasonal changes in river water levels (river stages) govern a wide range of hydrologic, geomorphological and ecological processes. Hydrologic modelling of the Amazon flood wave predicts discharge only along the main channel (the main stem), and suggests that up to 30% of mainstem flow exchanges with the flood plain⁷. On the basis of transport models, the annual sediment exchange between the main channel and flood plain is more than twice the flux through the most downstream river gauge at Obidos⁸. However, the models do not describe the sources or residence times of the floodplain water; these are key variables for measuring biological productivity and sedimentation. For example, observations of a small local catchment demonstrate that early in the water year, the lake contains nearly 70% river water whereas later in the water year, local runoff and other sources increase lake stage, preventing rising flood-stage river water from entering and exchanging with the lake⁹. Because very few of the ~8,000 Amazon floodplain lakes are gauged, the generality of these observations is unclear¹⁰.

Remotely sensed observations of the water surface provide an alternative to permanent gauging. Satellite radar altimetry promises a stage elevation accuracy of about 10 cm: but because altimetry is a profiling and not an imaging technique, it is applicable only to water